International Journal of Neural Systems, Vol. 28, No. 10 (2018) 1850031 (20 pages)

DOI: 10.1142/S0129065718500314

World Scientific
www.worldscientific.com

Neuronal Activation Detection Using Vector Phase Analysis with Dual Threshold Circles: A Functional Near-Infrared Spectroscopy Study

Amad Zafar* and Keum-Shik Hong†
School of Mechanical Engineering
Pusan National University, 2 Busandaehak-ro
Geumjeong-gu, Busan 46241, Korea
**amad@pusan.ac.kr*
†*kshong@pusan.ac.kr*

Accepted 21 June 2018
Published Online 25 July 2018

In this paper, a new vector phase diagram differentiating the initial decreasing phase (i.e. initial dip) and the delayed hemodynamic response (HR) phase of oxy-hemoglobin changes (ΔHbO) of functional near-infrared spectroscopy (fNIRS) is developed. The vector phase diagram displays the trajectories of ΔHbO and deoxy-hemoglobin changes (ΔHbR), as orthogonal components, in the ΔHbO–ΔHbR polar coordinates. To determine the occurrence of an initial dip, dual threshold circles (an inner circle from the resting state, an outer circle from the peak values of the initial dip and the main HR) are incorporated into the phase diagram for making decisions. The proposed scheme is then applied to a brain–computer interface scheme, and its performance is evaluated in classifying two finger tapping tasks (right-hand thumb and little finger) from the left motor cortex. Three gamma functions are used to model the initial dip, the main HR, and the undershoot in generating the designed HR function. In classifying two tapping tasks, the signal mean and signal minimum values during 0–2.5 s, as features of initial dip, are used. The linear discriminant analysis was utilized as a classifier. The experimental results show that the active brain locations of the two tasks were quite distinctive ($p < 0.05$), and moreover, spatially specific if using the initial dip map at 4 s in comparison to the map of HRs at 14 s. Also, the average classification accuracy was improved from 59% to 74.9% when using the phase diagram of dual threshold circles.

Keywords: Functional near-infrared spectroscopy (fNIRS); initial dip; brain–computer interface (BCI); motor cortex; vector phase analysis; neuronal firing; designed hemodynamic response function.

1. Introduction

To reduce erroneous detections of initial dips appearing in functional near-infrared spectroscopy (fNIRS) signals, this paper presents a systematic method using two threshold circles in the vector phase diagram. fNIRS is a noninvasive imaging method that uses near-infrared light within the 650–1000 nm range to measure the variations of regional cerebral blood flows (rCBFs) in the brain.[1,2] The two infrared light-absorbing chromophores in the blood are oxy-hemoglobin (HbO) and deoxy-hemoglobin (HbR).[3] Upon neuronal activities,[4] the concentration level of HbO/HbR in the capillaries and venules accompanied by dilation of pial arteries and arterioles increases/decreases, which is called the hemodynamic response (HR) that reflects the introduction of more oxygen to the brain.[5,6] In contrast to the HR, however, the initial dip denotes the consumption of oxygen at the time of neuronal activities, which reflects the early decreasing phenomenon of HbO.[7] Recently, the improvement of temporal resolution of fNIRS through the early detection of initial dip

†Corresponding author.

using vector phase analysis was reported.[8] The vector phase analysis is a polar coordinate plane method defined by oxy-hemoglobin changes (ΔHbO) and deoxy-hemoglobin changes (ΔHbR) as orthogonal vector components. Two other vector components, cerebral oxygen exchange (i.e. $\Delta\text{COE} = (1/\sqrt{2})(\Delta\text{HbR} - \Delta\text{HbO})$) and cerebral blood volume (i.e. $\Delta\text{CBV} = (1/\sqrt{2})(\Delta\text{HbO} + \Delta\text{HbR})$), can be defined to analyze the cerebral oxygenation and hemoglobin changes reflecting the neural activity at the same time.[9] Furthermore, to enhance the spatial resolution of fNIRS, the use of bundled-optode configuration was recently proposed.[10,11] Therefore, fNIRS has a great potential to be used as a viable neuroimaging tool, and its important applications include behavioral and cognitive neurodevelopment,[12] perception and cognition,[13] psychiatric conditions,[14] experimental psychology for language studies,[15] stroke and brain injury,[16] clinical and bedside imaging,[17] and brain–computer interfaces (BCIs).[18–22]

Hemodynamic signals (ΔHbO and ΔHbR) consist of the following three parts: (i) initial dip, (ii) main HR, and (iii) undershoot period.[23,24] Figure 1 shows the schematic of a typical normalized HR (i.e. generated by three gamma functions[25] assuming a 10 s task) depicting the initial dip, the main positive HR period, and the undershoot period. To examine the relative magnitudes of these responses, the peak values of initial dips and the main HRs from three brain cortices (prefrontal, motor, and visual) were compared in Ref. 26.

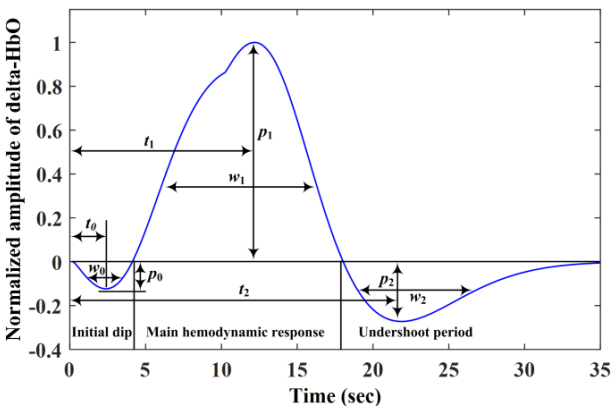

Examples of p_0 and p_1.[26]

Brain region	p_0 ($10^{-1}\mu$M)	p_1($10^{-1}\mu$M)	$\lvert p_0\rvert/p_1$
Prefrontal cortex	−0.57	1.97	0.29
Motor cortex	−0.89	3.37	0.27

Fig. 1. Schematic of a typical HR including the initial dip generated by three gamma functions assuming a 10 s task: t_0, t_1, and t_2 are the times to the peaks of initial dip, main HR, and undershoot; p_0, p_1, and p_2 are their peak values, and w_0, w_1, and w_2 are the durations for half peak values, respectively.

In the HR-based brain imaging, the detection of a neuronal activation in a particular brain region entails the determination of a specific time-series shape from the recorded hemodynamic signals.[27,28] In fNIRS, the existence of such a waveform is determined by the t-statistics analysis of the measured data to the time-series profile known as the canonical HR function (cHRF).[29] In such statistical analyses, the cHRF plays a key role, as its shape may vary among subjects, trials, and brain regions.[30] The most frequently utilized model of cHRF is the difference between two gamma functions that characterize the overall positive shape and the secondary undershoot in time series.[31,32] Then, the cHRF is further convolved with an experimental paradigm to generate the designed HR function (dHRF).[33,34] The dHRF is then fitted to measured HRs to find out the active channels (i.e. a brain region) showing high correlation to the dHRF. Then, a functional map can be drawn to depict a cortical brain region.[35,36] However, a key drawback in using two gamma functions in the estimation of dHRF is that it cannot account for the characteristics of the initial dip. To the best of our knowledge, no study has used a dHRF scheme including the initial dip for BCI purposes. Although, NIRS-SPM and functional optical signal analysis (fOSA) toolboxes provide three gamma functions as an option, it allows to incorporate the dynamics of the initial dip.[36,37]

The first focus in this paper is to develop a rigorous method in detecting the initial dip systematically, as it appears earlier in time than the conventional HR. Moreover, initial dips are spatially more specific to the neuron firing regions.[38,39] Kato *et al.*[40–43] carried out the first study in measuring the initial dips appearing in fNIRS signals from the motor, visual, and language areas. Later on, Jasdzewski *et al.*[24] further confirmed the presence of initial dips in fNIRS signals measured from the motor and visual cortices. They found that the HR was delayed by 2 s, which entails that the peak of

the initial dip exists within 2 s. They also observed that different parts in the brain behave differently in relation to the occurrence of initial dips. Kato[7] showed that NIRS has a high sensitivity to oxygen exchanges in capillaries. On that basis, he demonstrated that NIRS has the ability to measure the neural-response-related fast-oxygen response in capillaries, which was named the fast-oxygen response in capillary event (FORCE) rather than initial dip. Akiyama *et al.*[44] also found, within 1 s to 3 s of motor task initiation, distinctive biphasic responses in terms of cortical oxygenation (i.e. HbO) in the center of the primary motor cortex. Similarly, another study of Wylie *et al.*[45] examined the spatiotemporal co-variations among ΔHbO, ΔHbR, and total hemoglobin (ΔHbT ≈ ΔCBV) in the visual cortex for their contrast-reversing checkerboard experimental paradigm. They observed a decrease or an increase in ΔHbO/ΔHbR at the start of the activity which also demonstrates the consumption of oxygen at the time of neuronal activity (initial dip) prior to the main HR.

The first detection of an initial dip in fNIRS signals using a vector phase analysis method has been done by Yoshino and Kato.[46] A problem in their vector-based phase analysis is that an unrelated large fluctuation might be interpreted as an initial dip. Also, the detection time of an initial dip was not specified in the diagram. Hong and Naseer[8] improved the vector phase diagram[46] by integrating a threshold circle having the radius of $\max(\Delta\text{HbO}^2 + \Delta\text{HbR}^2)^{1/2}$ during the resting state. This circle has been used as a decision criterion for the occurrence of an initial dip. They also proposed to use an auto-regressive moving average model with exogenous input in combination with the vector phase analysis method to predict, q-steps ahead, the occurrence of initial dips and, thereby, reduce the time lag in detecting an initial dip to about 0.9 s. Recently, Zafar and Hong[26] have applied the initial dip detection method, by changing the threshold circle from $\max(\Delta\text{HbO}^2 + \Delta\text{HbR}^2)^{1/2}$ to $\max\{\Delta\text{HbO}, \Delta\text{HbR}\}$, to the classification problem of three mental tasks originated from the prefrontal cortex for BCI. They demonstrated that the moving window size in fNIRS-based BCI can be reduced to 2.5 s if using the proposed initial dip detection method (the previously suggested window duration was 5 s,[18] that is, from 2 s to 7 s from the onset time of a task). However, there still remains a possibility that any large ΔHbO/ΔHbR fluctuation greater than the threshold circle can be falsely interpreted as the occurrence of an initial dip.

In the present study, two disjoint regions (i.e. the initial dip region and the HR region) in the phase diagram, see Fig. 2, are separately defined as decision criteria to reduce possible false claims of initial dips in BCI applications (see Sec. 2). The use of a secondary threshold circle in addition to the primary threshold circle from the resting state is proposed. Furthermore, three gamma functions[25] are incorporated to generate a cHRF including the initial dip, the main HR, and the undershoot period to find active channels and to draw the activation map for online BCI applications. Outlining the obtained results in this work briefly, first an average increase of 15.9% in classification accuracy was observed by using the proposed criteria in comparison to the case of one threshold circle in the phase diagram. Second, the activation map drawn near the end of the initial dip period (i.e. at 4 s) demonstrates that the locations of the activated areas from two finger tapping tasks (i.e. right-hand thumb finger and right-hand litter finger) were more clearly distinguishable than that obtained by using the conventional HRs (at 14 s).

Three research issues in the BCI field are (i) how to enhance the classification accuracy; (ii) how to

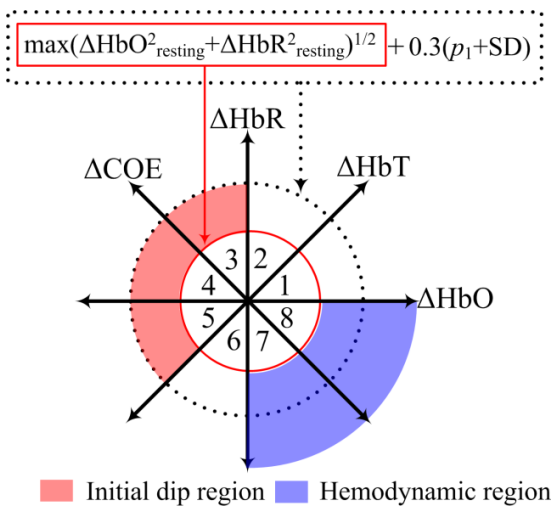

Fig. 2. Vector phase diagram with dual threshold circles indicating the initial dip phase and the HR phase, respectively.

increase the number of brain commands for improving the degrees of freedom of an external device, and (iii) how to quickly decode the brain commands by reducing the delay. In this paper, two issues are addressed: First, the initial dip detection will reduce the detection time. Second, since the initial dip is spatially specific to regional neuron firing, the generation of brain commands from a restricted brain region will become diverse, which consequentially results in an increased number of commands from a wider brain region. To demonstrate the second issue, a densely configured arrangement of optodes is applied to the left motor cortex, and a distinctive detection of two fingers (thumb, little fingers) has been experimented.

2. Methods

2.1. *Phase diagram with dual threshold circles*

The vector phase analysis is a systematic method utilizing the coordinates defined by the pair of ΔHbO and ΔHbR (or ΔCBV and ΔCOE) for detection of initial dips and HRs.[46] The vector components ΔCBV and ΔCOE are obtained by rotating the vector coordinate system defined by ΔHbO and ΔHbR by 45° counterclockwise using the following equations[47]:

$$\Delta\text{CBV} = \frac{1}{\sqrt{2}}(\Delta\text{HbO} + \Delta\text{HbR}), \tag{1}$$

$$\Delta\text{COE} = \frac{1}{\sqrt{2}}(\Delta\text{HbR} - \Delta\text{HbO}). \tag{2}$$

The magnitude and phase of a vector, $p = (\Delta\text{HbO}, \Delta\text{HbR})$, in this plane can be calculated as

$$|p| = \sqrt{\Delta\text{HbO}^2 + \Delta\text{HbR}^2}, \tag{3}$$

$$\angle p = \tan^{-1}\left(\frac{\Delta\text{HbR}}{\Delta\text{HbO}}\right) = \tan^{-1}\left(\frac{\Delta\text{COE}}{\Delta\text{CBV}}\right) + 45°. \tag{4}$$

The ratio of ΔCOE to ΔCBV (i.e. ΔCOE/ΔCBV) defines the degree of oxygen exchange. Therefore, ΔCOE represents the oxygen exchange in the blood vessels and thus also the neuronal activities.[48] $\Delta\text{COE} > 0$ representing deoxygenation in the capillaries as a result of oxygen consumption by the nerve cells. On the other hand, $\Delta\text{COE} < 0$ indicates that the oxygen-containing red blood cells are being supplied by the arteries and, thus, a high level of oxygenation in the blood vessels. The phase diagram is divided into eight phases/regions according to four components (ΔHbO, ΔHbR, ΔCBV, and ΔCOE). Table 1 summarizes the decomposition of the phase plane into eight phases/regions and their interpretations. Phases 1 to 5 in Table 1 are considered as initial dip phase as they are reflecting deoxygenation (i.e. an increase in either ΔHbR or ΔCOE). Therefore, an event-related vector residing in these regions are defined as an initial dip.[46] In Phases 1 and 2, both ΔCBV and ΔHbR are increasing, which are named as the canonical dip.[46,49] Phases 3 to 5 are the hypoxic dips with a decrease in ΔHbO together with increase/decrease in ΔCBV. These Phases (3 to 5) indicate the hypoxic change in blood vessels, thus representing deoxygenation in capillaries.[46–48] In Phases 6 to 8, both ΔHbR and ΔCOE are decreasing, therefore they are named as nondip phases.

The inner threshold circle in Fig. 2 (red solid circle) is to detect the time instance of the occurrence of an initial dip (in Phases 3–5) and the start of the HR (in Phases 7, 8) from the resting state. If there is

Table 1. Decomposition of the phase plane.[46]

Region	Conditions	Description
1	$0 < \Delta\text{HbR} < \Delta\text{HbO}$, $\Delta\text{COE} < 0 < \Delta\text{CBV}$	Canonical dip phase with $\Delta\text{COE} < 0$
2	$0 < \Delta\text{HbO} < \Delta\text{HbR}$, $0 < \Delta\text{COE} < \Delta\text{CBV}$	Canonical dip phase with $\Delta\text{COE} > 0$
3	$\Delta\text{HbO} < 0 < \Delta\text{HbR}$, $0 < \Delta\text{CBV} < \Delta\text{COE}$	
4	$\Delta\text{HbO} < 0 < \Delta\text{HbR}$, $\Delta\text{CBV} < 0 < \Delta\text{COE}$	Hypoxic dip phase with $\Delta\text{COE} > 0$
5	$\Delta\text{HbO} < \Delta\text{HbR} < 0$, $\Delta\text{CBV} < 0 < \Delta\text{COE}$	
6	$\Delta\text{HbR} < \Delta\text{HbO} < 0$, $\Delta\text{CBV} < \Delta\text{COE} < 0$	
7	$\Delta\text{HbR} < 0 < \Delta\text{HbO}$, $\Delta\text{COE} < \Delta\text{CBV} < 0$	Hyperoxia nondip phase with $\Delta\text{COE} < 0$
8	$\Delta\text{HbR} < 0 < \Delta\text{HbO}$, $\Delta\text{COE} < 0 < \Delta\text{CBV}$	

no threshold circle, a resting state fluctuation with $\Delta\text{COE} > 0$ can easily be interpreted as an initial dip. The radius of the first threshold circle is defined as follows:

$$r_1 = \max(\Delta\text{HbO}^2_{\text{resting}} + \Delta\text{HbR}^2_{\text{resting}})^{1/2}, \quad (5)$$

which is the maximum value during the resting state. However, there still remains a possibility that large fluctuations of ΔHbO and ΔHbR above the threshold circle during the task period can be interpreted as an initial dip. For this reason, based on our previous data,[26] the use of a secondary threshold circle (i.e. an outer circle as a bound for eliminating those ΔHbO fluctuations departing the region surrounded by the inner and outer circles in Phases 3–5) is proposed. To determine the radius of the outer circle, an empirical approach is used. In the experimental data of Zafar and Hong,[26] it was found that the ratio of the amplitude of initial dip (p_0) and that of the conventional HR amplitude (p_1) was about 0.3, see Fig. 1. Similar results were also reported in the previous studies of optical imaging spectroscopy and fMRI.[49–53] Therefore, once an experiment starts, the p_1 value and its standard deviation (SD) through the averaging over several trials from the most active channel in the training stage is determined, in which the most active channel means the channel that shows the largest difference between the maximum ΔHbO values during the resting state and the averaged HR during the training stage. Now, the second threshold circle is defined as follows:

$$r_2 = \max(\Delta\text{HbO}^2_{\text{resting}} + \Delta\text{HbR}^2_{\text{resting}})^{1/2} + 0.3(p_1 + \text{SD}). \quad (6)$$

The main reason for selecting p_1 in (6) for the secondary threshold circle is to make it independent from the occurrence of initial dip. In contrast, if we select $|p_0|$ (or $|p_0| + \text{SD}$) instead of $0.3p_1$ (or $0.3(p_1 + \text{SD})$), there exists a possibility that $|p_0|$ can become zero due to averaging. If $|p_0|$ becomes zero, the radius of the secondary circle will be r_1 or r_1+SD, which will result in overlapping (or too close) of the outer circle with the inner circle. Then, the role of the second circle is diminished by leading to a bad conclusion that a genuine initial dip is regarded as a false dip.

In the relevant previous research,[46–48] it was observed that most of the initial dips were of the hypoxic type (i.e. decreased ΔHbO). In the present analysis, Phases 3–5 represent the hypoxic dip phase in which $\Delta\text{COE} > 0$. The hypoxic initial dip region is then defined as the region between the two threshold circles in Phases 3–5, see Fig. 2. Similarly, the region outer the first threshold circle in Phases 7 and 8 is defined as the HR region. Therefore, the proposed criteria for detection of hypoxic initial dips are the following:

(i) the vector must lie in any of Phases 3–5, and

(ii) the trajectory should remain within the two threshold circles (i.e. the initial dip region). Any trajectory outside the initial dip region in Phases 3–5 is concluded as a false dip or noise. Also, if the trajectory remains in Phases 3–5 within first 2 s to 4 s period and it moves to either Phase 7 or 8, after 2 s to 4 s, having a magnitude greater than the circle drawn by the resting state hemodynamics (the first threshold circle), the trajectory is considered as a correct HR upon the given trial including the initial dip.

2.2. *BCI framework utilizing initial dip detection*

Figure 3 illustrates the proposed BCI framework incorporating the initial dip detection scheme discussed in Sec. 2.1. The main difference from the conventional scheme that uses the HRs is that even though the initial dip detection procedure fails, the conventional scheme still backs up. It is important to have a fail-tolerant loop in feature selection and classification for online control command generation. The existing fNIRS-based BCI framework uses only the HR features for classification, in which a typical window of 10 s from the stimulation onset is used to extract features. The commonly used HR features include the signal mean, signal peak, and signal slope during the 2–7 s duration, see details in Ref. 18. Though there are a few studies that have used the skewness, kurtosis, variance, SD, number of peaks, sum of peaks, and median for fNIRS-BCI, the use of initial dip does not exist yet. In the case of initial dip, the features should be extracted from the window of 0–2 s or 0–2.5 s. In this case, the previously mentioned features of HR may not work properly in a reduced window. The authors' previous work[26] examined five features of ΔHbO during the initial dip phase: Signal mean, signal minimum, signal peak, skewness, and kurtosis to classify multiple tasks from the prefrontal cortex in an offline analysis. The study found that the signal mean and the signal minimum

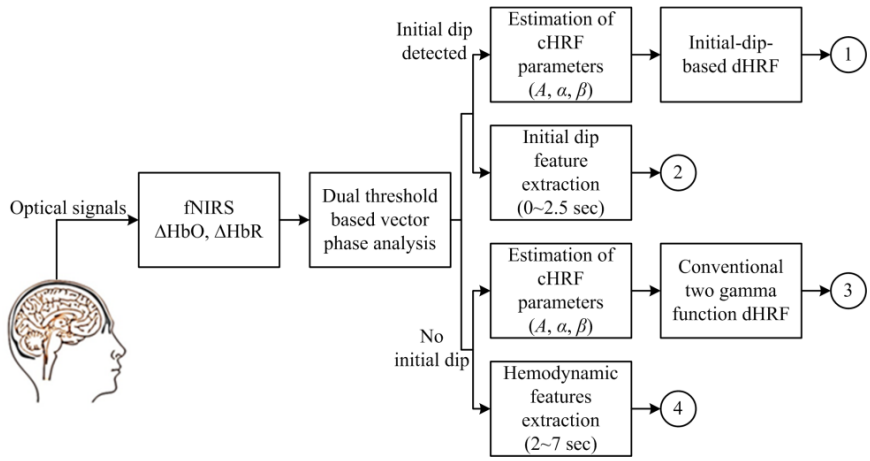

(a) Training scheme

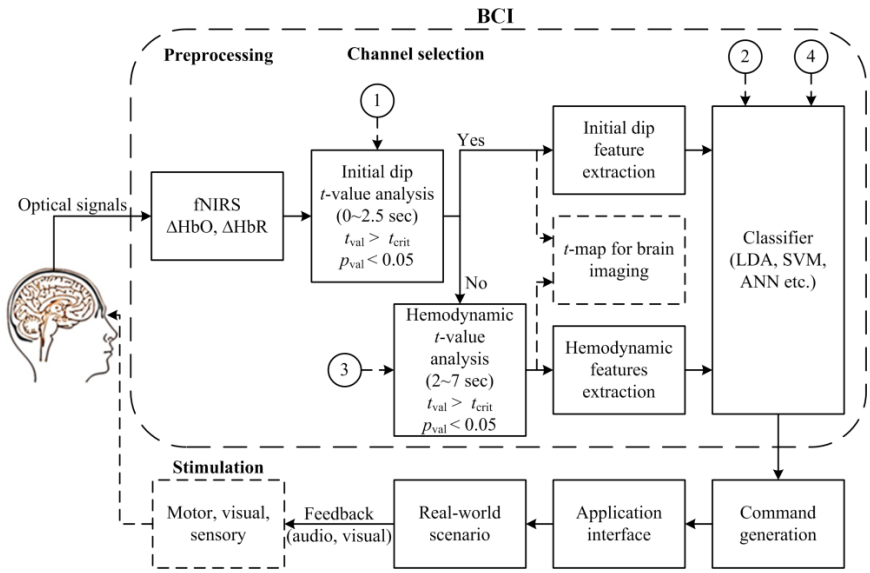

(b) Online scheme

Fig. 3. BCI framework using the vector phase diagram with dual threshold circles.

worked well with the 0–2.5 s window. Two other studies[54,55] have also investigated the early temporal features (signal minimum or signal mean) to utilize the initial dips in their early classification of multiple brain tasks. In this study, signal mean and signal minimum are used as features in the 0–2.5 s window, and the linear discriminant analysis (LDA) is used as a classifier.

2.3. *Subjects*

Eleven male subjects (age: mean 28.5 ± 2.5 years, hair style: shaved or very short hair) participated in the experiment. All were healthy and had normal or corrected-to-normal vision, and none had a history of any neurological or visual disorder. All were given a detailed description on the experimental procedure prior to the experiment, and informed consents were obtained from all. The experiment was conducted in accordance with the latest Declaration of Helsinki[56] upon the approval of the Pusan National University Institutional Review Board.

2.4. *Channel configuration and signal processing*

The brain signals generated by the tapping of two fingers (thumb, little fingers) were acquired at a

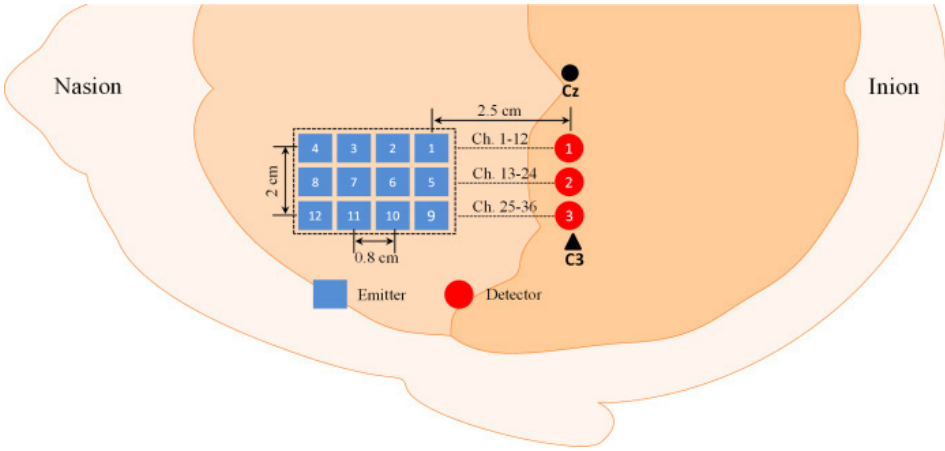

Fig. 4. Schematic of densely configured emitter–detector pairs in the left motor cortex.

sampling rate of 9.19 Hz from the left motor cortex using the frequency domain fNIRS system (ISS Imagent, ISS Inc.). The system utilizes the near-infrared light of two wavelengths (690 nm and 830 nm). In the present study, 3 detectors and 12 emitters were used in a dense emitter–detector configuration to examine the C3 area of the left motor cortex. The densely configured emitter–detector pairs helped to analyze the data of multi-distance channels obtained at various cortical depths resulting in an improved spatial resolution.[11] The electrode placement and the corresponding emitter-detector distances are shown in Fig. 4. In accordance with the International 10–20 System, the detectors were positioned by considering C3 as the reference point. Thirty-six channels were configured using emitter–detector combinations. ISS Imagent data acquisition and analysis software (ISS-Boxy) were used to obtain the raw intensity data. The intensity data were then converted to ΔHbO and ΔHbR with the ISS-Boxy software, with extinction coefficients $\varepsilon_{\mathrm{HbO}} = 0.95\,\mathrm{mM}^{-1}\mathrm{cm}^{-1}$, $\varepsilon_{\mathrm{HbR}} = 4.93\,\mathrm{mM}^{-1}\mathrm{cm}^{-1}$ for 690 nm wavelength and $\varepsilon_{\mathrm{HbO}} = 2.135\,\mathrm{mM}^{-1}\mathrm{cm}^{-1}$, $\varepsilon_{\mathrm{HbR}} = 1.791\,\mathrm{mM}^{-1}\mathrm{cm}^{-1}$ for 830 nm wavelength, according to the modified Beer–Lambert law.[57] The raw data (ΔHbO & ΔHbR) were pre-processed to remove the physiological noises related to the respiration, cardiac and low-frequency drift signals: A fourth-order Butterworth low- and high-pass filter with a cutoff frequency of 0.15 Hz and 0.01 Hz, respectively, was used to filter the respiration, cardiac, and low frequency drift fluctuations from the fNIRS signals.[54,58,59]

2.5. *Experimental paradigm*

Thumb and little finger tapping tasks associated with the left motor cortex were investigated. The subjects were seated on a comfortable chair and were instructed to avoid a body movement as much as possible during the experiment. The experiment was conducted in a dark and quite room. Figure 5 shows the experimental paradigm used in this study. One experiment consists of two sessions of tasks (thumb tapping, little finger tapping) with pre- and post-rest periods of 60 s and 10 s, respectively. Each session is composed of six 30 s trials. Each trial has a 10 s activity task followed by a 20 s rest. During the task period, the subjects were instructed to tap their (right) thumb/little fingers as fast as they could, without paying attention to the number of taps. A computer screen indicating individual finger tapping was displayed on a monitor placed in front of the

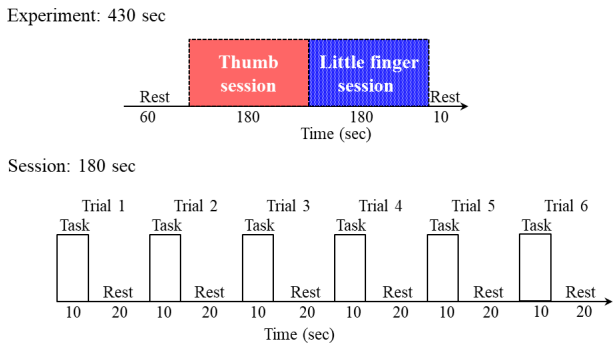

Fig. 5. Experimental paradigm for thumb and little finger tapping tasks.

subject. During the rest period, a black screen was shown. The subjects also were instructed to keep their eyes open during the experiment.

2.6. *Initial-dip-based dHRF and t-map generation*

In the fNIRS data analysis, the estimation of cortical activation and its localization are the most important steps. Cortical activation can be estimated by fitting the measured HR to the predefined dHRF,[60–62] and its existence can be concluded according to the t-values of the associated channels. In this paper, the t-values were computed using the *robustfit* function available in MATLAB$^{\text{TM}}$. Let $x_p^q \in R^{M\times 1}$ be the measured data at the pth channel for the qth trial, and M be the number of data per trial. Then, the linear regression model is defined as follows[34]:

$$x_p^q = \phi_p^q H_r + \psi_p^q \cdot 1 + \varepsilon_p^q, \tag{7}$$

where $H_r \in R^{M\times 1}$ is the dHRF, $1 \in R^{M\times 1}$ is a column vector of 1's to correct the offset of the baseline, ϕ is the unknown coefficient indicating the activity strength of the dHRF, ψ is the coefficient to compensate the baseline drift of the signal, and $\varepsilon \in R^{M\times 1}$ denotes the white Gaussian noise. Then, the coefficient ϕ is estimated as follows:

$$[\hat{\phi}_p^q, \text{stats}] = \text{robustfit}(H_r, x_p^q), \tag{8}$$

where $\hat{\phi}_p^q$ denotes the estimate of ϕ_p^q and stats refers to the statistical data including t-value, p-value, standard error, etc. The basic idea is to test the null hypothesis that the estimated parameter ($\hat{\phi}_p^q$) of the brain activity is equal to zero or not. In other words, to test whether the estimated value ($\hat{\phi}_p^q$) of the brain activity is greater or less than the critical t-value (t_{crt}) with statistical significance. The t-value[63] is calculated as follows:

$$t - \text{value} = \frac{\hat{\phi}_p^q}{\text{SE}(\hat{\phi}_p^q)}, \tag{9}$$

where SE stands for the standard error. A higher t-value means that the signal is highly correlated with the dHRF. In this study, t_{crt} was set to 1.65 according to the degrees of freedom (i.e. trial = 30 s, the number of data points $M = 30\times 9.19 = 275, M-1 = 274$).

In this study, the dHRF was generated by convolving the cHRF, denoted by $h(k)$, with a stimulus period, $u(k)$, as follows:

$$\text{dHRF}(k) = \sum_{n=0}^{k-1} h(n)u(k-n), \tag{10}$$

$$u(k) = \begin{cases} 1, & \text{if } k \in \text{task}, \\ 0, & \text{if } k \in \text{rest}, \end{cases} \tag{11}$$

where task and rest represent the task period and the rest period, respectively (task = 10 s and rest = 20 s in this study). The cHRF was generated as a linear combination of three gamma functions by the equation[25]

$$h(k) = \sum_{i=1}^{3} A_i \frac{k^{\alpha_i - 1}\beta_i^{\alpha_i} e^{-\beta_i k}}{\Gamma(\alpha_i)}, \tag{12}$$

where i represents the number of gamma functions, A_i is the amplitude, α_i and β_i tune the shape and the scale, respectively, and k is the time step. In this study, nine parameters of the cHRF were assumed as free parameters instead of using fixed parameters. For each subject, these free parameters were estimated in order to make the best fit of the dHRF shape to the HR data of the subject. The reason for using the estimated parameters instead of some fixed parameters is that the fNIRS signals vary from subject to subject due to their individual differences.[64]

The cHRF parameters were estimated using a modified constrained Nelder–Mead simplex algorithm that allows the use of constraints specified as parameter bounds.[65,66] The advantage of using this algorithm is that it minimizes the function without any derivative information.[67] We have used the *fminsearchbnd* function for parameters estimation.[68] The objective function was formulated as follows:

$$J = \sum_{k=1}^{N} \{y_{\text{HbO}}^j(k) - \text{dHRF}(k)\}^2, \tag{13}$$

where j represents the channel number. The above cost function was then minimized by applying the constraints and using the initial values as follows[25]:

$$\begin{aligned} &\min\ J(A_1, A_2, A_3, \alpha_1, \alpha_2, \alpha_3, \beta_1, \beta_2, \beta_3) \quad \text{such that} \\ &-5 \le A_1 \le 0, \quad 0 \le A_2 \le 15, \quad -10 \le A_3 \le 0, \\ &0 \le \alpha_1 \le 3, \quad 2 \le \alpha_2 \le 10, \quad 6 \le \alpha_3 \le 25, \\ &0.5 \le \beta_1 \le 2, \quad 0.5 \le \beta_2 \le 2, \quad 0 \le \beta_3 \le 1.5, \end{aligned} \tag{14}$$

$$\begin{aligned} &A_1 = -0.5, \quad A_2 = 6, \quad A_3 = -1, \\ &\alpha_1 = 1.5, \quad \alpha_2 = 7, \quad \alpha_3 = 16, \\ &\beta_1 = 1, \quad \beta_2 = 1, \quad \beta_3 = 1. \end{aligned} \tag{15}$$

One possible way to select the initial values of free parameters, for finding the solution of (13), is to choose the parameter values used to generate the fixed optimal dHRF.[36,63] However, we have used the initial values described in (15), because the convergence of the algorithm to the solution with these values was already verified in the literature.[25]

Several previous studies[69,70] have pointed out that HbO is more sensitive and more reliable than HbR. Therefore, we used only HbO signals for further analysis. To locate the active regions based on thumb and little finger tapping, the t-value for each channel was calculated for the averaged HbO trial. Similarly, the used dHRF was the averaged one over all subjects. The averaging was performed over all subjects and trials. The criteria for concluding activeness were: (i) t-value $> t_{\text{crt}}$ and (ii) p-value < 0.05. If the t-value $< t_{\text{crt}}$ or p-value > 0.05, the t-value was set to zero. The obtained t-values were normalized within the 0–1 range and were displayed on a t-map in order to illustrate an activation in the covered brain region. The active regions (the region of interest, ROI) were then defined as a region consisting of those channels whose t-values were higher than the t_{crt} for the performed task. To further confirm that the oxygen consumption was also increased during the initial dip phase, the t-maps for COEs were also drawn by computing the t-values between the measured ΔCOE with the negative of dHRF (i.e. $-$dHRF). In this study, the t-values were computed for two time intervals: 0–4 s and 0–14 s, respectively, to compare the activation map of the initial dip phase and that of the conventional HR. The reason for displaying t-maps for two different time durations is to verify that the t-map obtained at 4 s is spatially more specific than the t-map obtained at 14 s.

2.7. *Features extraction and classification*

We have compared the classification accuracies in two cases: (i) Using the vector phase analysis and (ii) using dHRFs. In case (i), in both single- and dual-threshold circle cases, the channels in which initial dips were detected were averaged for each given task. The mean and the minimum value of the averaged signal during the 0–2.5 s period were obtained for each task, in which the *mean* and *min* functions from MATLAB$^{\text{TM}}$ were used. It is noted that, in case (i), the activated channels were obtained from the vector phase analysis and dHRF was not used. In case (ii), the feature extraction is upon the fact that the three-gamma-function based dHRF has been optimized in the training period by using active channels (involving an initial dip), which were found by the dual threshold scheme. The active channels in case (ii) are found through the t-test (t-value $> t_{\text{crit}}$ and the p-value < 0.05) between the best-fit dHRF and the measured HR during 0–2.5 s. To compare the classification performance between the best-fit-initial-dip-based dHRF and the two-gamma-function based dHRF, the mean and the minimum value during the 0–2.5 s period were obtained for each task. In both cases (i) and (ii), the extracted features were then rescaled between 0 and 1 by the following equation[71]:

$$f' = \frac{f - \min(f)}{\max(f) - \min(f)}, \tag{16}$$

where $f \in R^n$ represents the original value of the feature, f' is the rescaled value between 0 and 1, $\max(f)$ is the maximum value, and $\min(f)$ is the minimum value. The rescaled features were then classified using the LDA.[72,73] To determine the classification accuracies, six runs of six-fold cross-validation were used. Six-fold cross-validation randomly breaks the data into six equal sets and uses five sets for training and one set for testing. The process was repeated six times, and the mean accuracy was obtained.[74–76]

3. Results

Figure 6 shows the vector phase analysis of the thumb and little finger tapping of Sub. 1 (Ch. 18) for all six trials using the proposed initial dip and HR regions. It can be seen that at the start of both tasks, the trajectory moves to the initial dip region and then goes to the HR region. The initial dip was not detected in Trials 5 and 6 of the thumb tapping and in Trial 5 of the little finger tapping tasks. But, it can be seen that their trajectories also cross the inner circle in Phase 8 indicating that they are still correct, which demonstrate the use of the regular HRs. Figure 7 shows some examples of the trajectories of false and no initial dips (Sub. 1, thumb tapping): Without the outer circle, initial dips would have been falsely identified. It is also observed that, in Ch. 7, see Fig. 7(a), the trajectory initially moved toward the HR region, but later moved back to the

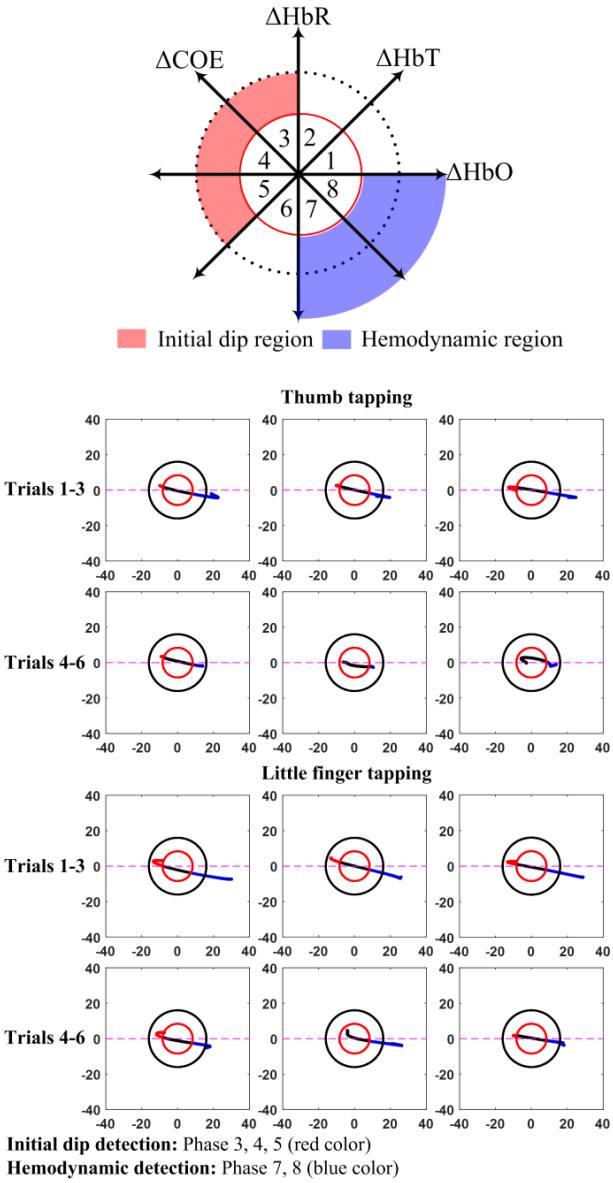

Fig. 6. (Color online) Trajectories of thumb and little finger tappings for a 10 s duration (Sub. 1, Ch. 18).

initial dip region causing a false signal. This kind of fluctuation might be due to artifacts (head movement, etc.); therefore, it would have been classified as an incorrect trial, but it was a correct trial with a large undershoot. On the other hand, these false dips would have been considered as initial dips according to the single threshold circle criterion. The channels in which initial dips and false dips were detected for the thumb tapping task of all the subjects are collected in Table 2.

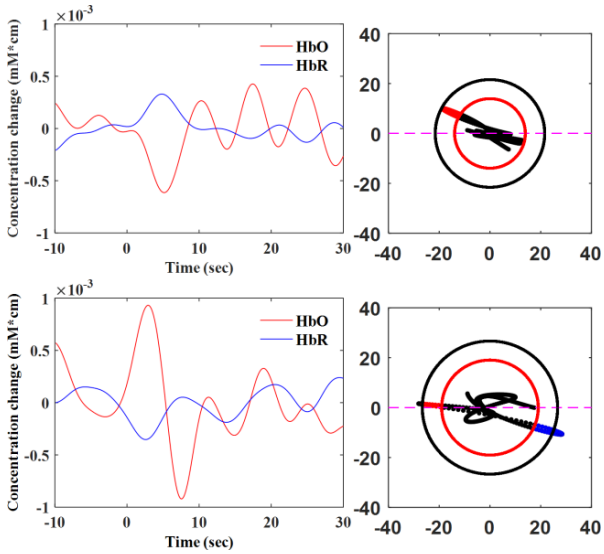

(a) False dip (the trajectory touches (Ch. 1, upper panel) and crosses the outer circle (Ch. 7, lower panel))

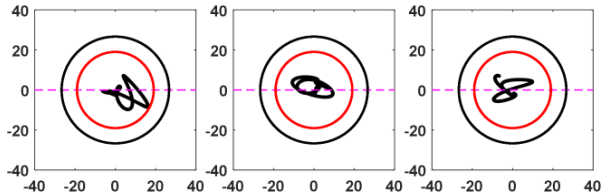

(b) No initial dip

Fig. 7. Examples of false and no initial dips.

Table 2. Comparison of thumb tapping analyses (single versus dual threshold circles).

Subject	Dual threshold circles: Correct channels	Dual threshold circles: False channels	Single threshold circle
1	17, 18, 21, 29, 30	1, 7	
2	18, 21, 29	3, 33, 36	
3	18, 21	4, 7, 15	
4	18, 21, 22, 29, 30	12	
5	33, 34	7, 11, 26	
6	13, 17, 18, 29, 33, 34	10, 16, 35	All channels shown in the left two columns are considered to have an initial dip
7	5, 17, 18, 21, 22, 23, 29, 30, 33, 34	10, 24, 31	
8	5, 17, 18, 21, 29, 33	1, 3, 20, 22, 28	
9	17, 21, 33	4, 6, 19, 32	
10	5, 13, 14, 17, 18, 21, 22, 23, 29, 30	3, 11, 12, 15, 19	
11	17, 18, 21, 22, 29, 33	9, 24, 30	

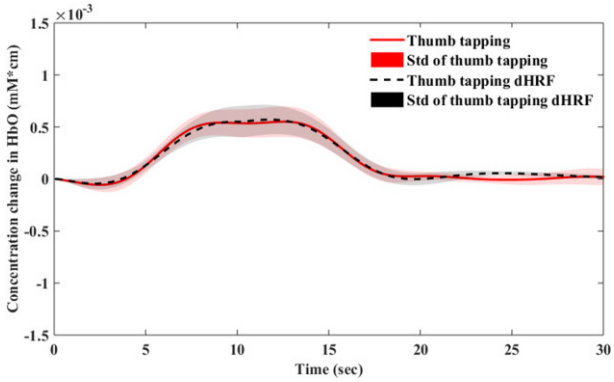

(a) Thumb tapping

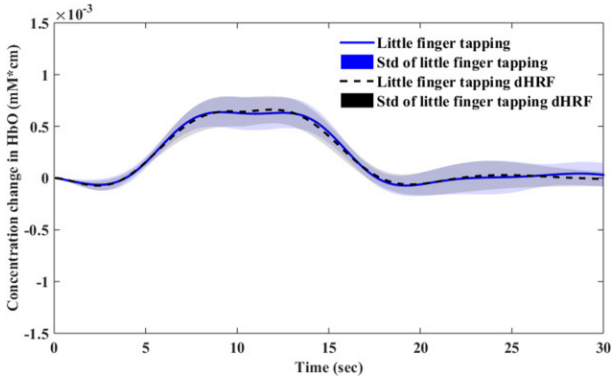

(b) Little finger tapping

Fig. 8. Mean (solid line) and SDs (shaded) of the measured data and the dHRF (dotted black line) generated by the estimated parameter values (Sub. 3).

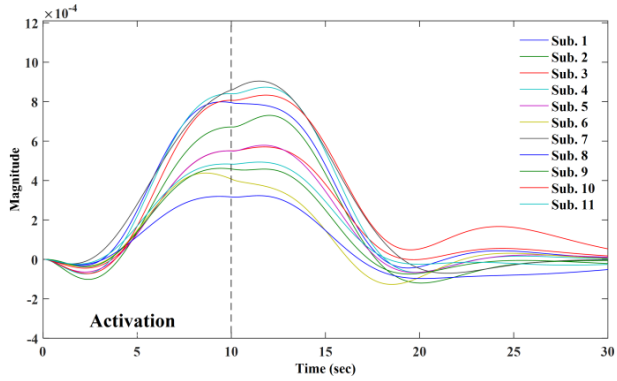

(a) Thumb tapping

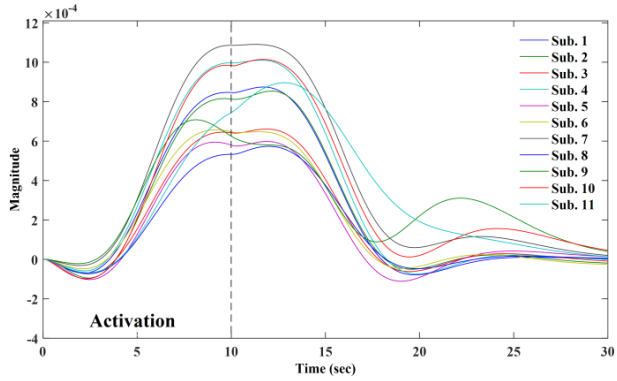

(b) Little finger tapping

Fig. 9. Comparison of the dHRFs of 11 subjects, which are generated by the estimated parameters (see appendix for the estimated cHRF parameters).

Figure 8 plots the averages and the SDs of the measured thumb and little finger tapping, respectively, and the corresponding dHRFs as generated by the estimated parameters of Sub. 3. Figure 9 compares the dHRFs generated using the estimated parameters for thumb and little finger tapping tasks (see Tables A.1 and A.2 containing the average values (over six trials) of the estimated parameters of the cHRFs, per subjects, for thumb and little finger tapping tasks).

Figure 10 plots the averaged HbOs (over 11 subjects and 6 trials) together with the SDs of the thumb and little finger tapping tasks. The shaded areas along the mean values represent the SDs. It is noted that the initial dip and the HR of the little finger tapping were stronger than those of the thumb tapping. The significance of the averaged HbOs was verified using two sample t-tests for initial dip (i.e. 4 s data, degree of freedom = 72 and $t_{\text{crt}} = -1.993$) and HR (i.e. 14 s data, degree of freedom = 256 and $t_{\text{crt}} = 1.969$). The *ttest2.m* function available in MATLAB$^{\text{TM}}$ was used. The experimental results demonstrate that the initial dip (t-value $= -2.07$ and

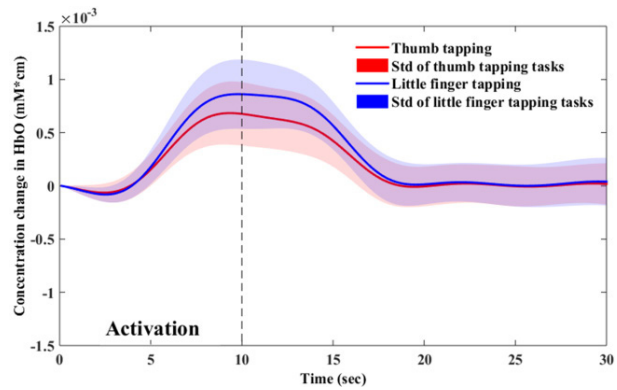

Fig. 10. Averaged HbOs (solid lines) and their SDs (shaded) of the thumb and little finger tapping tasks.

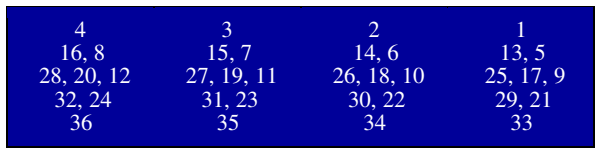

(a) Channels numbers denote the mid-points of individual emitter-detector distance.

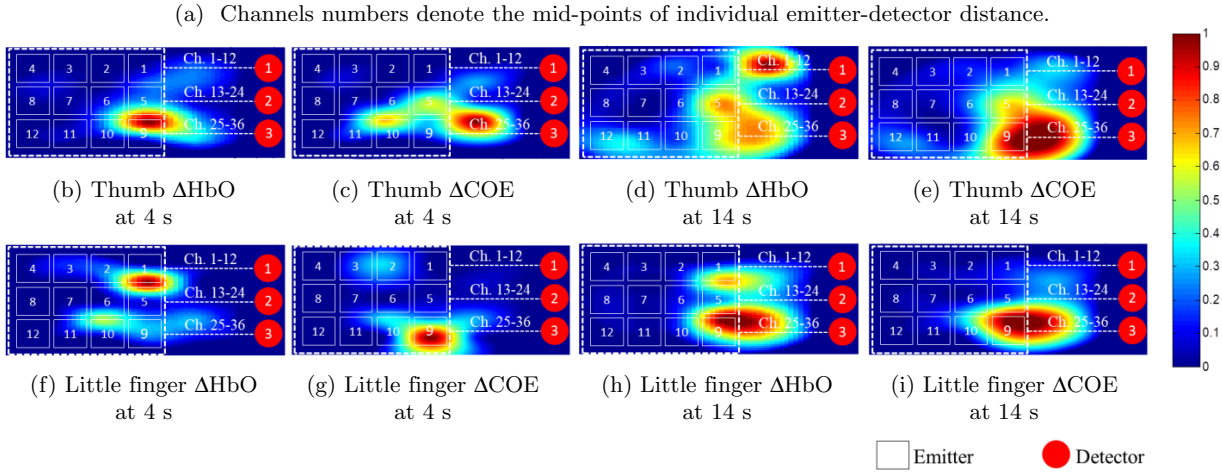

(b) Thumb ΔHbO at 4 s
(c) Thumb ΔCOE at 4 s
(d) Thumb ΔHbO at 14 s
(e) Thumb ΔCOE at 14 s
(f) Little finger ΔHbO at 4 s
(g) Little finger ΔCOE at 4 s
(h) Little finger ΔHbO at 14 s
(i) Little finger ΔCOE at 14 s

Fig. 11. Comparison of the t-maps at 4 s and 14 s of the HbOs and COEs averaged over all subjects and trials: $\Delta\text{HbO} < 0$ is seen at 4 s in (b) & (f), $\Delta\text{COE} > 0$ at 4 s in (c) & (g), $\Delta\text{HbO} > 0$ at 14 s in (d) and (h), and $\Delta\text{COE} < 0$ at 14 s in (e) and (f).

p-value = 0.041) and the HR (t-value = 2.29 and p-value = 0.022) of the thumb and little finger tapping tasks are different (p-value < 0.05).

Figure 11 compares the t-maps obtained using HbOs and COEs at 4 s and 14 s, respectively. It can be seen that the active spots of HbOs upon the little- and thumb-finger tapping tasks are clearly spatially distinguished (p-value < 0.05) in the case of 4 s window, see Figs. 11(b) and 11(f), in comparison with the case of 14 s window, see Figs. 11(d) and 11(h). Also, in Figs. 11(c) and 11(g), the oxygen consumption increases at 4 s ($\Delta\text{COE} > 0$) as compared to 14 s ($\Delta\text{COE} < 0$) in Fig. 11(e) and 11(i).

Table 3 reports the classification accuracies obtained after active channel selection by the vector phase analysis (single threshold circle, dual threshold circles) and dHRF (initial-dip-based and two gamma functions). To compare the significance of classification accuracies, we have used two sample t-tests (degree of freedom = 20, t_{crt} = 2.086). In comparison with the single threshold circle, the classification accuracy of dual circles was significantly increased from 59.0% to 74.9% (t-value = 4.613, p-value = $1.68e-04$). The classification accuracies of all subjects except Subs. 2, 5, and 10, were higher than the recommended classification accuracy needed for BCI (i.e. 70%). Similarly, the average classification accuracy obtained after active channel selection by the best-fit initial-dip-based dHRF, i.e. 72.7%, in a 2.5 s window was significantly higher than that obtained from the two gamma functions, i.e.

Table 3. Comparison of classification accuracies of thumb and little finger tapping tasks.

Classification accuracies (%) (Features: mean, min value; window: 0–2.5 s)				
Sub.	Single threshold circle	Dual threshold circles	Initial-dip-based dHRF	Two-gamma-functions-based dHRF
1	66.6	75	75	50
2	41.6	66.6	83.3	41.6
3	66.6	75	75	58.3
4	66.6	83.3	66.6	58.3
5	50	66.6	66.6	33.3
6	50	75	75	58.3
7	58.3	75	75	66.6
8	66.6	75	83.3	66.6
9	66.6	83.3	66.6	33.3
10	50	66.6	58.3	50
11	66.6	83.3	75	66.6
Mean	**59.0**	**74.9**	**72.7**	**55.9**
Std.	**9.4**	**6.4**	**7.5**	**12.5**

Table 4. Times required to process one to six trials using the proposed vector-phase analysis with dual threshold circles and initial-dip-based dHRF.

	Processing time (s)	
Trials	Dual threshold circle	Initial-dip-based dHRF
1	0.168	0.108
2	0.304	0.169
3	0.445	0.229
4	0.585	0.287
5	0.690	0.358
6	0.806	0.409

Table 5. Comparison of classification accuracies obtained from repeated experiments (Subs. 4 and 7).

Sub.	Classification accuracies (%) Channel selection: Initial-dip-based dHRF (Features: mean, min value; window: 0–2.5 s)				**Mean Std.**	
	Day 1		Day 2			
	Session 1	Session 2	Session 1	Session 2		
4	66.6	50	58.3	66.6	**60.3**	**7.9**
7	58.3	66.6	83.3	75	**70.8**	**10.7**

55.9% (t-value = 4.47, p-value = $2.31e-04$). There was no significant difference between the accuracies obtained using vector phase analysis with dual threshold circles and best-fit initial-dip-based dHRF (t-value = 0.75, p-value = 0.45). The processing times spent to process one to six trials using the dual vector phase analysis and initial-dip-based dHRF, respectively, are reported in Table 4. To further check the test–retest results of our proposed method, two subjects (Subs. 4 and 7) were asked to participate in more experiments. Four experiments were performed on each subject in two consecutive days (two sessions at different times per day). The best-fit initial-dip-dHRF of each subject (see Fig. 9) was used to select the active channels. Table 5 reports the classification accuracies obtained for four different experiments. The classification accuracy of Sub. 7 was higher than 60% in three sessions, which seems good enough and is acceptable for BCI.

4. Discussion

The novelties of this paper are the following: (i) new definitions of the initial dip and HR regions in the vector phase diagram to reduce false identification of initial dips in fNIRS signals, (ii) the use of a linear combination of three gamma functions to model the dHRF with initial dip to draw the initial-dip-based brain activation map and select active channels for fNIRS-BCI applications, and (iii) the demonstration of the capability of classifying two finger movements which are originated from a small brain region. This is possible because the initial dip is more specific to a brain region than the hemodynamics.

In this paper, the use of dual threshold circles to clarify the initial dip and HR regions in the vector phase diagram to detect the occurrence of initial dips in fNIRS signals is proposed for the first time. The early fNIRS studies used a single threshold circle having a radius of either $\max(\Delta\mathrm{HbO}^2 + \Delta\mathrm{HbR}^2)^{1/2}$ or $\max\{\Delta\mathrm{HbO}, \Delta\mathrm{HbR}\}$, as a decision criterion, from the resting state hemodynamics. Our work has an advantage over the early studies, as we were able to identify whether the dips are false or motion-related artifacts, which enhanced the classification accuracy for the BCI applications. We have used a 30% of the maximum value and its SD of the HR of an active channel in the decision of the radius of the second threshold circle because we had found in our previous study that the amplitude of the initial dip is almost 0.3 times that of the conventional HR.[26] This finding is consistent with optical imaging spectroscopy studies in which the early response is about 1/3 of the delayed response.[49–52] Later, an fMRI study reported that in the motor area, the ratio of the earlier response to the delayed response is roughly 0.3.[53] However, in the case of fMRI, it was also found that the ratio of the initial dip peak to the HR peak varies with the strength of the magnetic field of the fMRI system.[52,77] Furthermore, we used only Phases 3–5 to define the hypoxic initial dip region, because in the previous fNIRS studies as well as in our current study, it was observed that hypoxic-ischemic-type (i.e. decreased ΔHbO) initial dips frequently occurred.[26,46–48] Our proposed criteria worked well for all subjects, trials, and activity tasks. The peaks of the initial dips of all subjects and tasks remained within the initial dip region (see Fig. 6 of Sub. 1), which helped to identify and eliminate the false-dip channels.

In this paper, the use of a linear combination of three gamma functions (instead of two) for the detection of cortical activation as well as active channel

selection for BCI was also utilized. Several previous studies used a modified version of the existing two-gamma-function dHRF to analyze the fNIRS time series.[29,60] The advantage of using three gamma functions over two gamma functions is that it will also include the initial dip in the dHRF model for better estimation of the fNIRS signal. Also, the existing literature suggests that the fNIRS signals vary in their shape and characteristics from subject-to-subject and trial-to-trial.[64] In fact, it is evident in Fig. 9 that inter-subject differences existed in the cHRF parameters due to individual differences in anatomical factors. Therefore, the estimation of the dHRF shape of each subject for a better online-BCI channel selection was useful.

With regard to the active brain regions upon individual finger movements, the activation maps were drawn at the ends of 4 s and 14 s periods based on the averaged HbO and the initial-dip-based dHRF. Recalling that several previous studies indicated that the initial dip peaks occurred at around 2 s and finished at around 4 s,[24,52,78,79] the first t-map was drawn at 4 s, see Figs. 11(b) and 11(f), and another one at 14 s, see Figs. 11(d) and 11(h), in order to compare the active brain areas by using the initial dip and the conventional HR. It was found that the highly active locations of HbOs upon thumb and little-finger tapping were more spatially specific at 4 s than at 14 s. The 14 s t-map is more widely spread over the region. But, very distinctive activation locations for individual taps are shown in 4 s map. Similarly, in the case of COEs, the oxygen consumption in 4 s was also higher ($\Delta\text{COE} > 0$) and distinctive for both tasks in comparison to 14 s ($\Delta\text{COE} < 0$). This shows that the oxygen consumption during neuroactivation is higher in the dip phases as compared to HR phases, which is consistent with the existing literature.[46] Also, the HR of little finger tapping was stronger than that of thumb finger tapping. The obtained results are quite consistent with the previous relevant studies.[10,80–83] Even though the current results in initial-dip-based dHRF are preliminary, they will certainly contribute constructively to the fNIRS brain-imaging community.

In this study, the window size was chosen as 0–2.5 s, and the features used to classify thumb and little finger tapping tasks were the signal mean and the signal minimum value. Several previous studies have reported the occurrence of the initial dip peak at approximately 2–2.5 s.[44–46,52] Therefore, a 2.5 s window can provide the reliable classification accuracy in using the initial dips. The classification accuracy obtained by using the dual threshold circles for channel selection was significantly higher than that obtained with the single threshold circle (see Table 3). The reason for the low accuracy with the single threshold circle criterion (i.e. 59% in our case) is that it used all of the channels showing a magnitude greater than the maximum value in resting state hemodynamics. There is a possibility that during an activity period, some channels will show unexpected peaks due to unknown fluctuations. In the previous method, there is no criterion to identify those channels showing such false dips. The advantage of the second threshold circle is that it helps to eliminate those channels before the channel averaging for BCI applications, which results in a higher classification accuracy (i.e. 74.9% in this study). It is important to note that, for a channel to be selected as an active channel using the vector phase analysis with dual threshold circles, we have to wait till the trajectory enters the HR region (i.e. approximately 6 s to 7 s), which is too slow for the online applications. Also, it requires a computation time of 0.168 s and 0.806 s for one trial and six trials, respectively.

Finally, to address the above issue (i.e. delay of approximately 6 s to 7 s), we suggest using the best-fit initial-dip-based dHRF model for selection of active channels for the classification of the tapping task. The best-fit initial-dip-based dHRF yielded a higher classification accuracy, 72.7%, in a 2.5 s window than that of two gamma functions, 55.9%. In comparison with the vector phase analysis of dual threshold circles, the best-fit initial dip dHRF yielded a slightly lower classification accuracy (t-value = 0.75, p-value = 0.45), but it can reduce the delay time from 6 s to 2.5 s. Also, the computation time needed for processing of six trials is almost half (i.e. 0.409 s) of the processing time taken by the vector phase analysis (i.e. 0.806 s). The reduction in delay and overall processing time are a significant improvement toward real-time BCI applications using fNIRS.[54,84–88]

5. Limitations and Future Prospects

In this study, the value 0.3 for the ratio of $|p_0|$ to p_1 was adopted from the literature, which is

from empirical data. This ratio may depend on the tasks, measured locations, subjects, definition of initial dips, and the temporal resolution of the fNIRS system. Therefore, this ratio should be determined in the training phase by performing several trials for a given task. Once the training data are obtained, the ratio can be calculated based on the averaged data and its SD for the specific tasks, measured locations, and subjects. However, there exists a possibility that the initial dip may disappear by averaging. Specifically, in the case of initial dip disappearance, the ratio will be kept to 0.3 for the second threshold circle. Moreover, an optimal value of the ratio may exist, which can help to investigate the best possible radius of the threshold circles. Thus, it further enables us to investigate the vector phase analysis to be used as an independent classifier. We have considered hypoxic initial dips, however, other types of dips should also be considered in the future.

For the estimation of dHRF parameters, gamma functions were used to model the cHRF. The use of three gamma functions provides an extra degree of freedom in the estimation of dHRF including an initial dip. Previously, Ye *et al.*[36] had observed a significant increase in the correlation between the hemodynamic components (HbO, HbR, and HbT) and the dHRF approximated with multiple gamma functions (maximum 4 in their case). Therefore, multiple gamma functions in the estimation of a dHRF should be investigated for finding the best degree of freedom. Also, other functions like Gaussian model, half cosine functions, etc., deserve a further investigation.

It should also be noted that the densely configured emitter–detector pairs in our study contain only 12 emitters and 3 detectors, resulting in only 36 channels that can record brain activities only in a local brain region of 2 cm × 4.9 cm area. However, if more emitter/detector combinations are available for forming more channels that cover a wider brain region, more findings can be made. We have focused only on the activation map generated by the averaged signal over all subjects and trials. We were able to see that the t-maps of thumb and little fingers were distinguishable in some subjects, but not from all subjects. This is possibly due to two reasons: (i) the muscle motions of each finger are affected by each other[81] and (ii) the spatial resolution of our configuration was not sufficient to distinguish these overlapping regions. Therefore, a further investigation to improve the spatial resolution with a densely configured arrangement of optodes with closely placed emitter–detector pairs should be made.

In this study, we have used a Butterworth filter at a cutoff frequency of 0.15 Hz to reduce physiological noise. In this case, the HR caused by skin blood flow may be present, which may affect the features' value. However, it was shown in the previous study[89] that the correlated or uncorrelated information could enhance the overall classification accuracy as these features would work well for each other. In the future, it should be investigated that the improvement in classification accuracy can be achieved by using a skin blood flow removal technique. Another main limitation of fNIRS is the inter-subject and intra-subject variations in HRs due to physiological/psychological individual differences and trial-to-trial variability.[64,90,91] These individual differences can variate the threshold circle radii and the classification accuracies (as observed in Tables 3 and 5). For a clinical application, the variation in HRs can be minimized by averaging over trials per session. However, in the case of BCI, the variation in individual subjects (due to HRs variation) can be minimized by introducing additional features from a secondary modality (e.g. EEG). Therefore, the dip detection and accuracy improvement should be investigated by employing hybrid modalities.[92–94] Finally, we have used only temporal features from the HbO signals. In the future, other features (including HbR, COE, and CBV) should be investigated for further improvement of initial dip classification accuracy.

6. Conclusion

In this study, the vector phase analysis method with dual threshold circles was used to identify the false dips in the fNIRS signals. Also, the use of a three-gamma function to model initial-dip-based dHRF for active channel selection, identifying the active regions for the initial dip, and their application for BCI were demonstrated. Right-hand thumb and little finger tapping tasks associated with the left motor cortex were performed. The initial dip region in the vector phase analysis revealed that the initial dip can indeed be detected successfully and remain within this region. Our results demonstrated that by using

the initial-dip-based dHRF, the activation map for the initial dip (i.e. 4 s) can show highly active locations of tapping tasks more specifically and distinguishably than the activation map for the main HR (i.e. 14 s). We used temporal features with LDA-based classification to achieve 74.9% accuracy within the 0–2.5 s window with the dual threshold circles. In comparison with the single threshold circle, an average increase of 15.9% was observed. Also, the initial-dip-based dHRF, due to its shorter delay and processing time than that of vector phase analysis, yielded a higher classification accuracy than the commonly used two-gamma-function dHRF for an online application. These encouraging results show a greater potential of the initial-dip-based classification method for fNIRS-based BCI applications.

Acknowledgments

This work was supported by the National Research Foundation (NRF) of Korea under the auspices of the Ministry of Science and ICT, Republic of Korea (Grant Nos. NRF-2017R1A2A1A17069430 and NRF-2017R1A4A1015627).

Appendix

Table A.1. Averages of the estimated parameters of cHRF for thumb tapping task (over six trials).

	1st Γ			2nd Γ			3rd Γ		
Sub	A_1	α_1	β_1	A_2	α_2	β_2	A_3	α_3	β_3
1	−4.6E−06	1.8849	1.1206	2.8E−04	6.0836	0.6753	−1.9E−04	14.9801	1.4508
2	−1.9E−05	1.8848	1.1216	2.9E−04	6.0792	0.6752	−2.0E−04	14.9557	1.4513
3	−1.0E−05	1.9709	1.1497	1.5E−04	6.0857	0.7686	−8.9E−05	13.7450	1.4387
4	−8.7E−06	1.8834	1.1019	2.4E−04	6.0899	0.6934	−1.4E−04	15.5289	1.4329
5	−1.1E−05	1.8860	1.1244	2.0E−04	5.9398	0.6694	−1.3E−04	15.1059	1.4593
6	−4.5E−06	1.8802	1.1239	1.7E−04	6.0048	0.6740	−1.3E−04	14.8595	1.4558
7	−4.0E−06	1.4774	1.3338	1.2E−04	5.2271	0.7488	−3.2E−05	18.0041	1.4898
8	−5.3E−05	2.3609	0.5724	8.6E−05	4.2503	0.9202	−1.8E−05	20.6709	1.0017
9	−3.9E−06	1.9017	1.1140	1.3E−04	5.9138	0.6862	−8.5E−05	15.6304	1.4519
10	−1.2E−05	1.8833	1.1189	2.9E−04	6.1045	0.6761	−1.8E−04	14.9293	1.4503
11	−4.2E−06	2.0754	1.0735	8.9E−05	5.6422	0.8070	−3.5E−05	14.4542	1.4341

Table A.2. Averages of the estimated parameters of cHRF for little finger tapping task (over six trials).

	1st Γ			2nd Γ			3rd Γ		
Sub	A_1	α_1	β_1	A_2	α_2	β_2	A_3	α_3	β_3
1	−1.5E−05	1.8862	1.1954	2.1E−04	5.4101	0.6802	−1.1E−04	15.1609	1.4750
2	−1.6E−05	1.8836	1.1213	3.2E−04	6.0844	0.6746	−2.2E−04	14.9719	1.4513
3	−1.2E−05	1.8846	1.1211	2.6E−04	6.0818	0.6746	−1.8E−04	14.9513	1.4514
4	−1.6E−05	1.9253	1.1283	2.6E−04	5.7056	0.7159	−1.4E−04	14.7616	1.4630
5	−1.7E−05	1.8854	1.1253	2.5E−04	5.9335	0.6708	−1.8E−04	14.9495	1.4605
6	−1.4E−05	1.9721	1.0843	2.1E−04	5.7295	0.7268	−1.3E−04	13.7830	1.4427
7	−6.0E−06	1.8998	1.1434	3.5E−04	6.2377	0.7016	−2.1E−04	14.9294	1.4650
8	−1.3E−05	1.8820	1.1260	2.1E−04	5.9572	0.6699	−1.3E−04	14.9636	1.4593
9	−4.5E−06	1.8970	1.1237	4.1E−04	6.1241	0.6581	−3.1E−04	14.0625	1.4631
10	−1.5E−05	1.8906	1.1331	2.8E−04	6.0308	0.6853	−1.6E−04	15.3705	1.4553
11	−1.3E−05	1.8863	1.1217	2.1E−04	6.0491	0.6768	−9.8E−05	14.9411	1.4531

References

1. A. Pellicer and M. Del Carmen Bravo, Near-infrared spectroscopy: A methodology–focused review, *Semin. Fetal Neonatal Med.* **16**(1) (2011) 42–49.
2. H. Santosa, M. J. Hong, S.-P Kim and K.-S. Hong, Noise reduction in functional near-infrared spectroscopy signals by independent component analysis, *Rev. Sci. Instrum.* **84**(7) (2013) 073106.
3. M. Cope and D. T. Delpy, System for long-term measurement of cerebral blood and tissue oxygenation on newborn-infants by near-infrared trans-illumination, *Med. Biol. Eng. Comput.* **26**(3) (1998) 289–294.
4. F. Montani, A. Oliynyk and L. Fadiga, Superlinear summation of information in premotor neuron pairs, *Int. J. Neural Syst.* **27**(2) (2017) 1650009.
5. T. Kato, A. Kamei, S. Takashima and T. Ozaki, Human visual cortical function during photic stimulation monitoring by means of near infrared spectroscopy, *J. Cereb. Blood Flow Metab.* **13** (1993) 516–520.
6. A. Villringer, J. Planck, C. Hock, L. Schleinkofer and U. Dirnagl, Near infrared spectroscopy (NIRS): A new tool to study hemodynamic changes during activation of brain function in human adults, *Neurosci. Lett.* **154**(1–2) (1993) 101–104.
7. T. Kato, Principle and technique of NIRS imaging for human brain FORCE: Fast-oxygen response in capillary event, *Int. Cong. Ser.* **1270** (2004) 85–90.
8. K.-S. Hong and N. Naseer, Reduction of delay in detecting initial dips from functional near-infrared spectroscopy signals using vector-based phase analysis, *Int. J. Neural Syst.* **26**(3) (2016) 1650012.
9. K. Yoshino, N. Oka, K. Yamamoto, H. Takahashi and T. Kato, Correlation of prefrontal cortical activation with changing vehicle speeds in actual driving: A vector-based functional near-infrared spectroscopy study, *Front. Hum. Neurosci.* **7** (2013) 895.
10. H.-D. Nguyen, K.-S. Hong and Y.-I. Shin, Bundled-optode method in functional near-infrared spectroscopy, *PLoS One* **11**(10) (2016) e0165146.
11. H.-D. Nguyen and K.-S. Hong, Bundled-optode implementation for 3D imaging in functional near-infrared spectroscopy, *Biomed. Opt. Express* **7**(9) (2016) 3491–3507.
12. H. Watanabe, Y. Shitara, Y. Aoki, T. Inoue, S. Tsuchida, N. Takahashi and G. Taga, Hemoglobin phase of oxygenation and deoxygenation in early brain development measured using fNIRS, *Proc. Natl. Acad. Sci. USA* **114**(9) (2017) E1737–E1744.
13. S. Cutini, S. Basso Moro and S. Bisconti, Functional near infrared optical imaging in cognitive neuroscience: An introductory review, *J. Near Infrared Spectrosc.* **20**(1) (2012) 75–92.
14. K. Ohi, T. Shimada, H. Kihara, T. Yasuyama, K. Sawai, Y. Matsuda, K. Oshima, H. Okubo, Y. Nitta, T. Uehara and Y. Kawasaki, Impact of familial loading on prefrontal activation in major psychiatric disorders: A near-infrared spectroscopy (NIRS) study, *Sci. Rep.* **7** (2017) 44628.
15. J. Gervain, Near-infrared spectroscopy: Recent advances in infant speech perception and language acquisition research, *Front. Psychol.* **5** (2014) 916.
16. P. E. Grant, N. Roche-Labarbe, A. Surova, G. Themelis, J. Selb, E. K. Warren, K. S. Krishnamoorthy, D. A. Boas and M. A. Franceschini, Increased cerebral blood volume and oxygen consumption in neonatal brain injury, *J. Cereb. Blood Flow Metab.* **29**(10) (2009) 1704–1713.
17. M. Ferrari, J. P. Culver, Y. Hoshi and H. Wabnitz, Clinical near-infrared spectroscopy and imaging of the brain, *Neurophotonics* **3**(3) (2016) 031401.
18. N. Naseer and K.-S. Hong, fNIRS-based brain–computer interfaces: A review, *Front. Hum. Neurosci.* **9** (2015) 3.
19. A. Ortiz-Rosario and H. Adeli, Brain–computer interface technologies: From signal to action, *Rev. Neurosci.* **24**(5) (2013) 537–552.
20. A. Ortiz-Rosario, I. Berrios-Torres, H. Adeli and J. A. Buford, Combined corticospinal and reticulospinal effects on upper limb muscles, *Neurosci. Lett.* **561** (2014) 30–34.
21. A. Burns, H. Adeli and J. A. Buford, Brain–computer interface after nervous system injury, *Neuroscientist* **20**(6) (2014) 639–651.
22. A. Ortiz-Rosario, H. Adeli and J. A. Buford, Wavelet methodology to improve single unit isolation in primary motor cortex cells, *J. Neurosci. Methods* **246** (2015) 106–118.
23. R. B. Buxton, E. C. Wong and L. R. Frank, Dynamics of blood flow and oxygenation changes during brain activation: The balloon model, *Magn. Reson. Med.* **39**(6) (1998) 855–864.
24. G. Jasdzewski, G. Strangman, J. Warner, K. K. Kwong, R. A. Poldrack and D. A. Boas, Differences in the hemodynamic response to event-related motor and visual paradigms as measured by near-infrared spectroscopy, *Neuroimage* **20**(1) (2003) 479–488.
25. Z. Y. Shan, M. J. Wright, P. M. Thompson, K. L. McMahon, G. G. Blokland, G. I. De Zubicaray, N. G. Martin, A. A. Vinkhuyzen and D. C. Reutens, Modeling of the hemodynamic responses in block design fMRI studies, *J. Cereb. Blood Flow Metab.* **34**(2) (2014) 316–324.
26. A. Zafar and K.-S. Hong, Detection and classification of three-class initial dips from prefrontal cortex, *Biomed. Opt. Express* **8**(1) (2017) 367–383.
27. K. Ciftci, B. Sankur, Y. P. Kahya and A. Akin, Constraining the general linear model for sensible hemodynamic response function waveforms, *Med. Biol. Eng. Comput.* **46**(8) (2008) 779–787.
28. T. J. Huppert, S. G. Diamond, M. A. Franceschini and D. A. Boas, HomER: A review of time-series

analysis methods for near-infrared spectroscopy of the brain, *Appl. Opt.* **48**(10) (2009) D280–D298.
29. A. F. Abdelnour and T. Huppert, Real-time imaging of human brain function by near-infrared spectroscopy using an adaptive general linear model, *Neuroimage* **46**(1) (2009) 133–143.
30. K.-S. Hong and H.-D. Nguyen, State-space models of impulse hemodynamic responses over motor, somatosensory, and visual cortices, *Biomed. Opt. Express* **5**(6) (2014) 1778–1798.
31. K. J. Friston, P. Fletcher, O. Josephs, A. Holmes, M. D. Rugg and R. Turner, Event-related fMRI: Characterizing differential responses, *Neuroimage* **7**(1) (1998) 30–40.
32. M. A. Lopez-Gordo, D. Sanchez-Morillo and M. A. J. Van Gerven, Spreading codes enables the blind estimation of the hemodynamic response with short-event sequences, *Int. J. Neural Syst.* **25**(1) (2015) 1450035.
33. M. A. Lindquist, L. J. Meng, L. Y. Atlas and T. D. Wager, Modeling the hemodynamic response function in fMRI: Efficiency, bias and mis-modeling, *Neuroimage* **45**(1) (2009) S187–S198.
34. H. Santosa, M. J. Hong and K.-S. Hong, Lateralization of music processing with noise in the auditory cortex: An fNIRS study, *Front. Behav. Neurosci.* **8** (2014) 418.
35. K.-S. Hong and H. Santosa, Decoding four different sound categories in the auditory cortex using functional near-infrared spectroscopy, *Hear. Res.* **333** (2016) 157–166.
36. J. C. Ye, S. Tak, K. E. Jang, J. W. Jung and J. D. Jang, NIRS-SPM: Statistical parametric mapping for near-infrared spectroscopy, *Neuroimage* **44**(2) (2009) 428–447.
37. P. H. Koh, D. Glaser, G. Flandin, S. Kiebel, B. Butterworth, A. Maki, D. T. Delpy and C. E. Elwell, Functional optical signal analysis: A software tool for near-infrared spectroscopy data processing incorporating statistical parametric mapping, *J. Biomed. Opt.* **12**(6) (2007) 064010.
38. M. Watanabe, A. Bartels, J. H. Macke, Y. Murayama and N. K. Logothetis, Temporal jitter of the BOLD signal reveals a reliable initial dip and improved spatial resolution, *Curr. Biol.* **23**(21) (2013) 2146–2150.
39. E. Yacoub and X. Hu, Detection of the early negative response in fMRI at 1.5 Tesla, *Magn. Reson. Med.* **41**(6) (1999) 1088–1092.
40. T. Kato, A. Endo, M. Fukumizu, T. Kato, S. Takashima, F. Kawaguchi and N. Ichikawa, Initial cerebral metabolism due to short visual stimulation using human functional near-infraredgraphy (fNIR): How it correlates with fMRI? in *Proc. 7th Annual Meeting of Int. Soc. Magnetic Resonance in Medicine* (International Society of Magnetic Resonance in Medicine, Philadelphia, 1999), p. 762.
41. T. Kato, A. Endo, M. Fukumizu, T. Kato, S. Takashima, F. Kawaguchi and N. Ichikawa, Real-time imaging of "Initial cerebral metabolism" using human functional near-infraredgraphy (fNIR), *Neuroimage* (1999) S309.
42. T. Kato, A. Endo, M. Fukumizu, J. Furusho, S. Takashima, F. Kawaguchi and N. Ichikawa, Single finger movement trial using human functional near-infraredgraphy (fNIR), *Neuroimage* (1999) S430.
43. T. Kato, Y. Yamashita, A. Maki, T. Yamamoto and H. Koizumi, Temporal behaviour of human functional near-infraredgraphy (fNIR) using single-word speaking trial, *Neuroimage* (1999) S1025.
44. T. Akiyama, T. Ohira, T. Kawase and T. Kato, TMS orientation for NIRS-functional motor mapping, *Brain Topogr.* **19**(1–2) (2006) 1–9.
45. G. R. Wylie, H. L. Graber, G. T. Voelbel, A. D. Kohl, J. DeLuca, Y. Pei, Y. Xu and R. L. Barbour, Using co-variations in the Hb signal to detect visual activation: A near infrared spectroscopic imaging study, *Neuroimage* **47**(2) (2009) 473–481.
46. K. Yoshino and T. Kato, Vector-based phase classification of initial dips during word listening using near-infrared spectroscopy, *Neuroreport* **23**(16) (2012) 947–951.
47. M. Sano, S. Sano, N. Oka, K. Yoshino and T. Kato, Increased oxygen load in the prefrontal cortex from mouth breathing: A vector-based near-infrared spectroscopy study, *Neuroreport* **24**(17) (2013) 935–940.
48. N. Oka, K. Yoshino, K. Yamamoto, H. Takahashi, S. Li, T. Sugimachi, K. Nakano, Y. Suda and T. Kato, Greater activity in the frontal cortex on left curves: A vector-base fNIRS study on left and right curve driving, *PLoS One* **10**(5) (2015) e0127594.
49. D. Malonek and A. Grinvald, Interactions between electrical activity and cortical microcirculation revealed by imaging spectroscopy: Implications for functional brain mapping, *Science* **272**(5261) (1996) 551–554.
50. R. D. Frostig, E. E. Lieke, D. Y. Ts'o and A. Grinvald, Cortical functional architecture and local coupling between neuronal activity and the microcirculation revealed by *in vivo* high-resolution optical imaging of intrinsic signals, *Proc. Natl. Acad. Sci. USA* **87**(16) (1990) 6082–6086.
51. A. Grinvald, R. D. Frostig, R. M. Siegel and E. Bartfeld, High-resolution optical imaging of functional brain architecture in the awake monkey, *Proc. Natl. Acad. Sci. USA* **88**(24) (1991) 11559–11563.
52. X. Hu and E. Yacoub, The story of the initial dip in fMRI, *Neuroimage* **62**(2) (2012) 1103–1108.
53. E. Yacoub and X. Hu, Detection of the early decrease in fMRI signal in the motor area, *Magn. Reson. Med.* **45**(2) (2001) 184–190.
54. M. J. Khan and K.-S. Hong, Hybrid EEG-fNIRS-based eight-command decoding for BCI: Application to quadcopter control, *Front. Neurorobot.* **11** (2017) 6.
55. R. Li, T. Potter, W. Huang and Y. Zhang, Enhancing performance of a hybrid EEG-fNIRS system using

channel selection and early temporal features, *Front. Hum. Neurosci.* **11** (2017) 462.
56. B. Christie, Doctors revise declaration of Helsinki, *Br. Med. J.* **321**(7266) (2000) 913–913.
57. D. T. Delpy, M. Cope, P. Van Der Zee, S. Arridge, S. Wray and J. Wyatt, Estimation of optical pathlength through tissue from direct time of flight measurement, *Phys. Med. Biol.* **33**(12) (1988) 1433–1442.
58. T. Fekete, D. Rubin, J. M. Carlson and L. R. Mujica-Parodi, The NIRS analysis package: Noise reduction and statistical inference, *PLoS One* **6**(9) (2011) e24322.
59. J. M. Kainerstorfer, A. Sassaroli, K. T. Tgavalekos and S. Fantini, Cerebral autoregulation in the microvasculature measured with near-infrared spectroscopy, *J. Cereb. Blood Flow Metab.* **35**(6) (2015) 959–966.
60. X.-S. Hu, K.-S. Hong, S. S. Ge and M. Y. Jeong, Kalman estimator- and general linear model-based online brain activation mapping by near-infrared spectroscopy, *Biomed. Eng. Online* **9** (2010) 82.
61. K.-S. Hong, M. R. Bhutta, X. Liu and Y.-I. Shin, Classification of somatosensory cortex activites using fNIRS, *Behav. Brain Res.* **333** (2017) 225–234.
62. X. Liu and K.-S. Hong, Detection of primary RGB colors projected on a screen using fNIRS, *J. Innov. Opt. Health Sci.* **10** (2017) 1750006.
63. K. J. Friston, J. T. Ashburner, S. J. Kiebel, T. E. Nichols and W. D. Penny, *Statistical Parametric Mapping*: *The Analysis of Functional Brain Images* (Elsevier, London, 2007).
64. X.-S. Hu, K.-S. Hong and S. S. Ge, Reduction of trial-to-trial variability in functional near-infrared spectroscopy signals by accounting for resting-state functional connectivity, *J. Biomed. Opt.* **18**(1) (2013) 017003.
65. M. A. Luersen and R. L. Riche, Globalized Nelder–Mead method for engineering optimization, *Comput. Struct.* **82**(23–26) (2004) 2251–2260.
66. J. A. Nelder and R. Mead, A simplex method for functional minimization, *Comput. J.* **7** (1965) 308–313.
67. J. C. Lagarias, J. A. Reeds, M. H. Wright and P. E. Wright, Convergence properties of Nelder–Mead simplex method in low dimension, *SIAM J. Optimiz.* **9**(1) (1998) 112–147.
68. Mathworks, Bound constrained optimization toolbox (2012). Retrieved from http://www.mathworks.com/matlabcentral/fileexchange/8277.
69. Y. Hoshi, Functional near-infrared optical imaging: Utility and limitations in human brain mapping, *Psychophysiology* **40**(4) (2003) 511–520.
70. Y. Hoshi, Functional near-infrared spectroscopy: Current status and future prospects, *J. Biomed. Opt.* **12**(6) (2007) 062106.
71. M. J. Khan and K.-S. Hong, Passive BCI based on drowsiness detection: An fNIRS study, *Biomed. Opt. Express* **6**(10) (2015) 4063–4078.
72. N. Naseer, F. M. Noori, N. K. Qureshi and K.-S. Hong, Determining optimal feature-combination for LDA classification of functional near-infrared spectroscopy signals in brain–computer interface application, *Front. Hum. Neurosci.* **10** (2016) 237.
73. M. P. Xu, J. Liu, L. Chen, H. Z. Qi, F. He, P. Zhou, B. K. Wan and D. Ming, Incorporation of inter-subject information to improve the accuracy of subject-specific P300 classifiers, *Int. J. Neural Syst.* **26**(3) (2016) 1650010.
74. J. Shin, K.-R. Muller and H.-J. Hwan, Near-infrared spectroscopy (NIRS)-based eyes-closed brain–computer interface (BCI) using prefrontal cortex activation due to mental arithmetic, *Sci. Rep.* **6** (2016) 36203.
75. F. Z. Xu, W. D. Zhou, Y. L. Zhen, Q. Yuan and Q. Wu, Using fractal and local binary pattern features for classifcation of ECOG motor imagery tasks obtained from the right brain hemisphere, *Int. J. Neural Syst.* **26**(6) (2016) 1650022.
76. Y. Zhang, Y. Wang, J. Jin and X. Y. Wang, Sparse Bayesian learning for obtaining sparsity of EEG frequency bands-based feature vectors in motor imagery classification, *Int. J. Neural Syst.* **27**(2) (2017) 1650032.
77. E. Yacoub, A. Shmuel, J. Pfeuffer, P.-F. Van De Moortele, G. Adriany, K. Ugurbil and X. Hu, Investigation of the initial dip in fMRI at 7 tesla, *NMR Biomed.* **14**(7–8) (2001) 408–412.
78. T. Ernst and J. Hennig, Observation of a fast response in functional MR, *Magn. Reson. Med.* **32**(1) (1994) 146–149.
79. D. S. Kim, T. Q. Duong and S. G. Kim, High-resolution mapping of iso-orientation columns by fMRI, *Nat. Neurosci.* **3**(2) (2000) 164–169.
80. J. Diedrichsen, T. Wiestler and J. W. Krakauer, Two distinct ipsilateral cortical representations for individuated finger movements, *Cereb. Cortex* **23**(6) (2013) 1362–1377.
81. J. D. Meier, T. N. Aflalo, S. Kastner and M. S. A. Graziano, Complex organization of human primary motor cortex: A high-resolution fMRI study, *J. Neurophysiol.* **100**(4) (2008) 1800–1812.
82. C. A. Olman, K. A. Pickett, M. P. Schallmo and T. J. Kimberley, Selective BOLD responses to individual finger movement measured with fMRI at 3T, *Hum. Brain Mapp.* **33**(7) (2012) 1594–1606.
83. J. C. W. Siero, D. Hermes, H. Hoogduin, P. E. Luijten, N. F. Ramsey and N. Petridou, BOLD matches neuronal activity at the mm scale: A combined 7 T fMRI and ECoG study in human sensorimotor cortex, *Neuroimage* **101** (2014) 177–184.
84. U. Chaudhary, B. Xia, S. Silvoni, L. G. Cohen and N. Birbaumer, Brain–computer interface-based communication in the completely locked-in state, *PLoS Biol.* **15**(1) (2017) e1002593.
85. T. Gateau, G. Durantin, F. Lancelot, S. Scannella and F. Dehais, Real-time state estimation in a

flight simulator using fNIRS, *PloS One* **10**(3) (2015) e0121279.
86. M. F. Li, W. Li and H. H. Zhou, Increasing N200 potentials via visual stimulus depicting humanoid robot behavior, *Int. J. Neural Syst.* **26**(1) (2016) 1550039.
87. A. R. Sereshkeh, R. Trott, A. Bricout and T. Chau, Online EEG classification of covert speech brain–computer interfacing, *Int. J. Neural Syst.* **27**(8) (2017) 1750033.
88. E. W. Yin, T. Zeyl, R. Saab, D. W. Hu, Z. T. Zhou and T. Chau, An auditory-tactile visual saccade-independent P300 brain–computer interface, *Int. J. Neural Syst.* **26**(1) (2016) 1650001.
89. S. Fazli, S. J. Mehnert, J. Steinbrink, G. Curio, A. Villringer, K.-R. Muller and B. Blankertz, Enhanced performance by a hybrid NIRS-EEG brain–computer interface, *Neuroimage* **59**(1) (2012) 519–529.
90. T. Yarkoni and T. S. Braver, Cognitive neuroscience approaches to individual differences in working memory and executive control: Conceptual and methodological issues, in *Handbook of Individual Differences in Cognition*: *Attention*, *Memory and Executive Control* eds. A. Gruszka, G. Matthews and B. Szymuyra (Springer, New York, 2010), pp. 87–107.
91. H. Sato, Y. Fuchino, M. Kiguchi, T. Katura, A. Maki, T. Yoro and H. Koizumi, Intersubject variability of near-infrared spectroscopy signals during sensorimotor cortex activation, *J. Biomed. Opt.* **10** (2005) 44001.
92. K.-S. Hong and M. J. Khan, Hybrid-BCI techniques for improved classification accuracy and increased number of commands: A review, *Front. Neurorobot.* **11** (2017) 35.
93. M. J. Khan, M. J. Hong and K.-S. Hong, Decoding of four movement directions using hybrid NIRS-EEG brain–computer interface, *Front. Hum. Neurosci.* **8** (2014) 244.
94. Y. Liu, H. Ayaz and P. A. Shewokis, Multisubject "learning" for mental workload classification using concurrent EEG, fNIRS, and physiological measures, *Front. Hum. Neurosci.* **11** (2017) 389.